Full length article

Microstructural controls on the plastic consolidation of porous brittle solids

Lars Blatny [a],*, Henning Löwe [b], Johan Gaume [a,b,c,d]

[a] *School of Architecture, Civil and Environmental Engineering, Swiss Federal Institute of Technology, Lausanne (EPFL), CH-1015 Lausanne, Switzerland*
[b] *WSL Institute for Snow and Avalanche Research SLF, CH-7260 Davos Dorf, Switzerland*
[c] *Institute for Geotechnical Engineering, ETH Zürich, CH-8093 Zürich, Switzerland*
[d] *Climate Change, Extremes, and Natural Hazards in Alpine Regions Research Center CERC, CH-7260 Davos Dorf, Switzerland*

ARTICLE INFO

ABSTRACT

Through stochastic-numerical microstructure-based experiments, the plastic consolidation under compression of porous brittle solids, with porosities from 0.25 to 0.75 and a large variety of microstructural characteristics, has been investigated. This was made possible by generating microstructures from Gaussian random fields in order to obtain stochastic ensembles of structures with prescribed properties, which are then simulated within the material point method. Below a critical imposed strain rate, the consolidation behavior is found to be very weakly affected by the degree of heterogeneity and anisotropy. Structures where the solid phase takes up more space than the void phase have a consolidation response approximately independent of the structural geometry and dimensionality (comparing two- and three-dimensional structures). Finally, we show that the consolidation of two-dimensional structures collapses on a single master curve that can be described by a simple function similar to one presented for a completely different system, namely a system of interacting discrete cohesive disks. In this function, we report a universal parameter largely independent of material specifications.

1. Introduction

The complex mechanics of porous (quasi-)brittle solids, such as various types of rocks, snow, ceramics, wood and bone, is crucial to the understanding of, for example, earthquakes [1], avalanches [2], design of functional materials [3,4] and in orthopedics [5]. The mechanical behavior of these solids depends on their microstructure. In the past, elastic and yield properties have been well studied through various microstructure-based models. With simplifying material assumptions or geometries, analytical considerations for such small strain behavior are possible, including the well known results by Hashin and Shtrikman [6], Gurson [7], Gibson and Ashby [8], Castañeda [9]. Later, various researchers have relied on microstructures obtained from X-ray tomography or from artificial approaches simulated with numerical schemes such as the finite element method (FEM) [10–14], the discrete element method (DEM) [15,16], the material point method (MPM) [17], or even a double-scale DEM-FEM coupling [18,19], to uncover more accurate mechanical relationships with the microstructural properties. However, their results are usually only related to the material's porosity, not accounting for the vast morphological variability the microstructure can display for the same porosity value. Furthermore, these approaches have been mostly limited to small strain mechanics, rarely going beyond failure or closer to the densification phase.

When compressing further after failure, porous materials display a mechanical regime generally characterized by an overall slowly increasing stress state until densification, at which point the stress increases drastically due to no available void space which the material can occupy. For soils, this consolidation phase has been well studied, where the so-called normal compression line gives a linear relationship between the specific volume (i.e., the inverse solid volume fraction) and the logarithm of the pressure [20,21]. In this linear relationship, the proportionality factor is coined the (plastic) compressibility or, compression index, with a numerical value depending on the type of soil. In fact, such relationship was found already in the first quarter of the last century from compaction experiments of powder samples [22]. For loose and cohesive granular systems such as powders, this index has been studied experimentally and computationally. For example, experiments on iron powders showed that the index depends on the initial solid fraction and yield stress [23], and experiments on different toners revealed it increases with the cohesion between the particles [24]. Moreover, recent numerical experiments of systems of randomly distributed sticky spheres found no effect by the solid volume fraction and stickiness of the granules on the compression index [16]. On the other hand, for cellular solids (with solid fractions less than 0.3), the pore collapse region between yield and densification is generally associated with a constant stress plateau, and the experimentally observed stress

---

* Corresponding author.
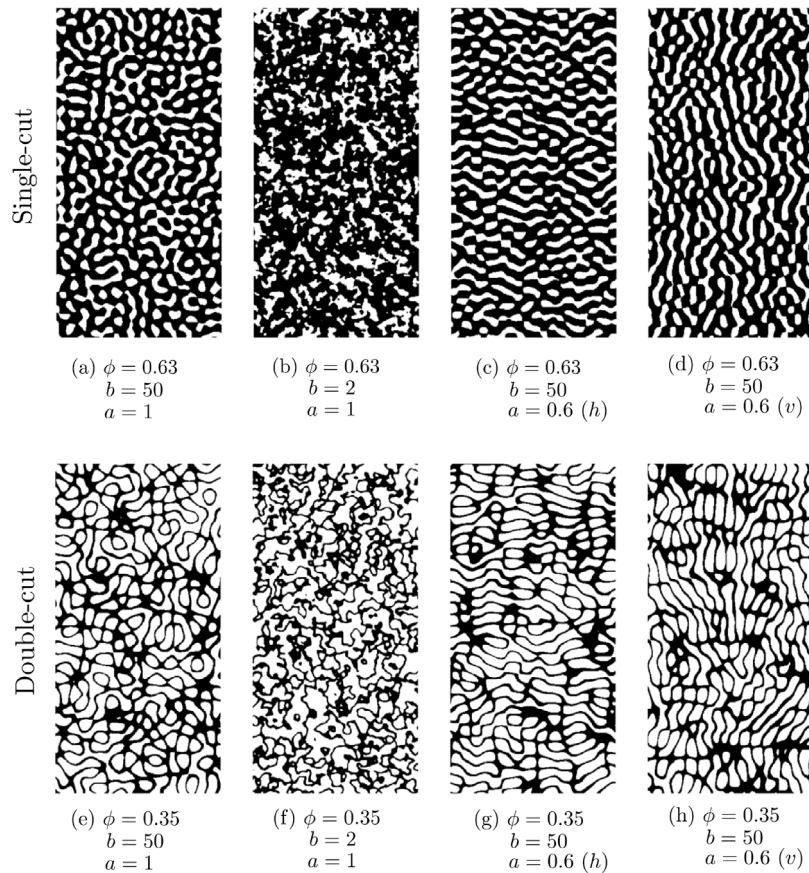 *E-mail address:* lars.blatny@epfl.ch (L. Blatny).

Fig. 1. Various microstructure geometries generated with Eq. (1) in the top row (a–d) and Eq. (2) in the bottom row (e–h). From left to right, the microstructures are isotropic and homogeneous (a, e), isotropic and heterogeneous (b, f) and anisotropic and homogeneous (c, d, g, h). The latter case is either with a vertically (marked v) or horizontally (marked h) preferred orientation.

increase is sometimes considered a result of the trapped pore gas pressure [25].

The question remains to what extent these previous results for soils, granular systems and highly porous cellular solids are also valid for generic porous brittle solids. In this work, the (post-failure, pre-densification) consolidation region is investigated for such materials with solid fractions between 0.25 and 0.75. While experimental investigations are possible, they are usually material-specific and become time-consuming when a significant number of samples are to be tested. On the other hand, numerical investigations allow for a systematic analysis of many possible geometries and material properties. Here, stochastic microstructures are generated from Gaussian random fields, allowing the control of a variety of structural properties independently. Combined with the material point method (MPM), we are able to simulate the complete compression of these continuous (non-particulate) structures while avoiding mesh distortion issues of classical finite elements. This combination represents an appropriate framework for probing the influence of the microstructural geometry on the mechanical properties under large, plastic, deformations.

2. Methods

2.1. Gaussian random field microstructures

Two-phase (binary) microstructures can be obtained efficiently by level-cutting Gaussian random fields (GRF) constructed to provide certain prescribed structural properties. Dating back to Cahn [26], this approach has been used in several studies of both electromagnetic and
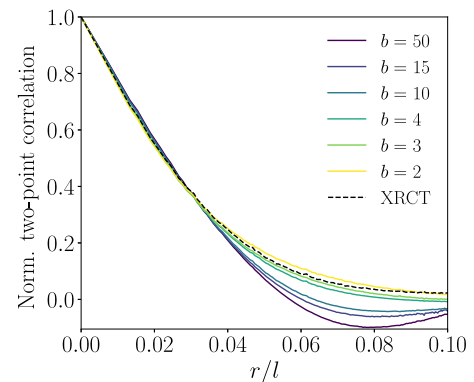

Fig. 2. Normalized two-point correlation function for a real snow microstructure obtained with XRCT and different GRF-structures of varying heterogeneity b. The correlation function is plotted as a function of distance r relative to the side length l of the cubic structures.

elastic properties of porous structures [17,27–30]. Given a Gaussian random field $G(\mathbf{r})$, a *single-cut* microstructure $M(\mathbf{r})$ is obtained by level-cutting $G(\mathbf{r})$ to the desired solid volume fraction ϕ,

$$M(\mathbf{r}) = \begin{cases} 1, & \text{if } G(\mathbf{r}) > \text{erf}^{-1}(1 - 2\phi) \\ 0, & \text{otherwise} \end{cases} \qquad (1)$$

such that $M(\mathbf{r}) = 1$ means $\mathbf{r}$ is in the solid phase and $M(\mathbf{r}) = 0$ means it is in the void phase. A *double-cut* structure can be obtained in a similar
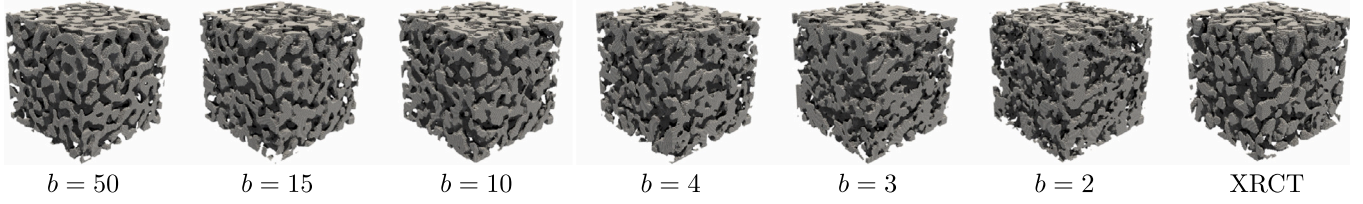
Fig. 3. Visualization of GRF-structures with varying degree of heterogeneity and a real snow microstructure obtained with XRCT.

way,

$$M(\boldsymbol{r}) = \begin{cases} 1, & \text{if } \mathrm{erf}^{-1}(-\phi) < G(\boldsymbol{r}) < \mathrm{erf}^{-1}(\phi) \\ 0, & \text{otherwise} \end{cases} \tag{2}$$

In both cases, $\mathrm{erf}^{-1}(\cdot)$ denotes the inverse error function and $G(\boldsymbol{r})$ is created as a superposition of $N_c \gg 1$ sinusoidal waves,

$$G(\boldsymbol{r}) = \frac{1}{\sqrt{N_c}} \sum_{n=1}^{N_c} \cos(\boldsymbol{\eta}_n \cdot \boldsymbol{r} + \varphi_n) \tag{3}$$

where the φ_n are independent, identically distributed random variables in $[0, 2\pi]$ and $\boldsymbol{\eta}_n$ are the wave vectors. Single-cut structures are characterized by thick grains connected by neck regions of smaller thickness, while double-cut structures form snaky paths with roughly the same thickness throughout which meet at several denser intersection points. Double-cut structures are always guaranteed to percolate while single-cut structures have a percolation threshold around $\phi = 0.15$ in three dimensions, and around $\phi = 0.5$ in two dimensions.

The magnitude and direction of the wave vectors $\boldsymbol{\eta}_n$ must be sampled according to the desired heterogeneity and anisotropy, respectively, of the microstructure. Following Ding et al. [27], the wave vector's magnitude $\eta \equiv 2\pi/\omega$ can be sampled from the gamma distribution function

$$P(\eta) = \frac{(b+1)^{(b+1)}}{\langle\eta\rangle\Gamma(b+1)} \left(\frac{\eta}{\langle\eta\rangle}\right)^b e^{-(b+1)\frac{\eta}{\langle\eta\rangle}} \tag{4}$$

where $\langle\eta\rangle$ is a prescribed mean wave vector magnitude and the parameter $b \in (0, \infty)$ controls the width of the distribution, in other words, the heterogeneity of the structure. A large value $b \gg 1$ results in an approximately homogeneous structure. To obtain isotropic microstructures, the wave vector directions are sampled uniformly over the unit sphere. For anisotropic structure, the sampling can be restricted to a subset of the unit sphere [28]. Here, we consider only structures with either horizontally or vertically preferred directions. To this end, we introduce an anisotropy parameter $a \in (0, 1]$ that quantifies the fraction of the unit sphere being sampled from. In particular, for two-dimensional vertically-aligned structures, we sample the polar angle uniformly from $[-a\pi/2, a\pi/2] \cup [\pi(1 - a/2), \pi(1 + a/2)]$. Fig. 1 illustrates various types of structures that can be generated in two dimensions.

2.2. Comparison to a real microstructure

It is instructive to consider if the artificial GRF-structures can reproduce real microstructures. To this end, a real snow microstructure has been obtained from X-ray micro-computed tomography (XRCT). This snow sample has a solid fraction of $\phi = 0.42$ and is nearly isotropic. By generating equally porous and isotropic single-cut GRF-microstructures of varying heterogeneity, we compare their two-point correlation function with that of the snow sample. This is presented in Fig. 2 from which it can be observed that a structure with heterogeneity parameter $b = 3$ provides a similar two-point correlation as the real snow structure. The various structures are visualized in Fig. 3.

2.3. Constitutive model of the solid phase

We consider the solid phase material as elastoplastic, i.e., with reversible deformations until the stress state reaches a yield criterion marking the onset of permanent, irreversible, deformations. A multiplicative decomposition of the deformation gradient tensor is assumed, i.e.,

$$\boldsymbol{F} = \frac{\partial\boldsymbol{x}}{\partial\boldsymbol{X}} = \boldsymbol{F}^E\boldsymbol{F}^P \tag{5}$$

where $\boldsymbol{F}^E$ refers to the deformation arising from the elastic forces, while $\boldsymbol{F}^P$ is the irreversible, plastic, component. Here, $\boldsymbol{X}$ denotes the coordinate in the initial configuration, and $\boldsymbol{x}$ is the deformed coordinate. As a convenient measure of strain, we will in this work rely on the Hencky strain,

$$\boldsymbol{\varepsilon} = \frac{1}{2}\ln(\boldsymbol{F}\boldsymbol{F}^T) = \frac{1}{2}\sum_{i=1}^d \ln \Lambda_i^2\ \boldsymbol{n}_i \otimes \boldsymbol{n}_i = \sum_{i=1}^d \ln \Lambda_i\ \boldsymbol{n}_i \otimes \boldsymbol{n}_i \tag{6}$$

where Λ_i and $\boldsymbol{n}_i$ are the principle stretches and (Eulerian) directions, respectively, in d dimensions. We require a constitutive relation between the stress and the elastic part of the deformation. In this work, we adopt an isotropic model known as the Hencky model, which results in the Kirchhoff stress $\boldsymbol{\tau}$ being related to the Hencky strain through

$$\boldsymbol{\tau} = L\,\mathrm{tr}(\boldsymbol{\varepsilon}^E)\boldsymbol{I} + 2G\boldsymbol{\varepsilon}^E \tag{7}$$

where $L = \frac{Ev}{(1+v)(1-2v)}$ and $G = \frac{E}{2(1+v)}$ are the two Lamé parameters related to the Young's modulus E and Poisson's ratio v. Note the elastic part of the Hencky strain is defined as $\boldsymbol{\varepsilon}^E = \frac{1}{2}\ln(\boldsymbol{F}^E(\boldsymbol{F}^E)^T)$. As shown by Xiao and Chen [31], the model given by Eq. (7) is hyperelastic, and the Kirchhoff stress and the Hencky strain constitute a work-conjugate pair. It is a model which has been successfully used in various studies [17,32–34] of large deformation modeling with MPM.

A yield criterion should reflect at least three common properties of porous brittle (geo)materials: (1) they usually consist of a solid phase that is pressure-dependent, (2) the solid phase typically displays an asymmetry in tensile and compressive strengths, and finally (3) they exhibit strong post-failure softening. In order to satisfy these properties in a simple manner, we make use of a strain-softening Drucker–Prager yield criterion for the solid phase of the microstructures, given by

$$y(p, q) = q - \gamma\left(p + ce^{-\xi\varepsilon_S^P}\right) \le 0, \tag{8}$$

expressed in the space of the mean stress $p = -\frac{1}{d}\mathrm{tr}\,\boldsymbol{\tau}$ and the von Mises equivalent stress $q = \sqrt{\frac{3}{2}\mathrm{dev}\,\boldsymbol{\tau} : \mathrm{dev}\,\boldsymbol{\tau}}$ which are stress invariants. Here, we introduced the deviatoric operator $\mathrm{dev}(\cdot) = (\cdot) - \frac{1}{d}\mathrm{tr}(\cdot)\boldsymbol{I}$. The three parameters of the yield criterion are $c \ge 0$ which characterizes the initial cohesion, $\gamma > 0$ which controls the friction and $\xi \ge 0$ giving the degree of post-yield softening. Note that softening is here controlled by the accumulated amount of deviatoric plastic Hencky strain $\varepsilon_S^P \equiv \sqrt{\mathrm{dev}(\boldsymbol{\varepsilon}^P) : \mathrm{dev}(\boldsymbol{\varepsilon}^P)}$. The friction γ can be related to the material's so-called friction angle φ_f,

$$\gamma = \frac{2d\sin\varphi_f}{3 - \sin\varphi_f} \tag{9}$$

Assuming the rate of work per unit undeformed volume can be additively decomposed into an elastic and plastic part, we have
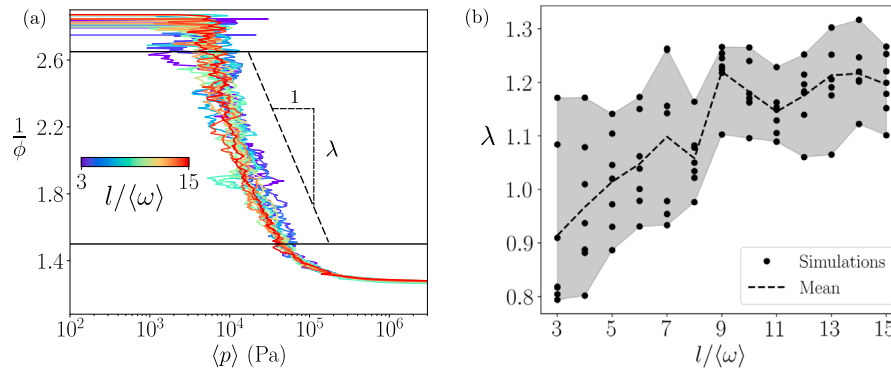
Fig. 4. Representative volume element analysis of a two-dimensional double-cut structure with $\phi_0 = 0.35$, $b = 50$ and $a = 1$. In (a), one simulation for each size $l/\langle\omega\rangle$ is shown, highlighting the region in which we fit a linear consolidation slope λ. In (b), the evolution of λ with increasing system size is shown. The stapled line is the mean of the individual simulation results represented by black dots.

$\tau : l = \tau : l^E + \tau : l^P$, where we defined an elastic and plastic part of the velocity gradient l. The latter, l^P is chosen through a plastic flow rule, in particular here given by a von Mises plastic potential, i.e.,

$$l^P = \dot{\gamma} \frac{\partial q}{\partial \tau} \tag{10}$$

where we introduced the plastic multiplier $\dot{\gamma}$. As such, this is a non-associative plastic flow rule similar to the one presented in Blatny et al. [17] and induces no plastic volumetric deformation. However, stress states $p < -ce^{-\xi \epsilon_S^P}$ require a special treatment, and are in this work projected to the tip of the Drucker–Prager cone. More details on this are presented in Appendix A. In addition to the previously stated condition $y \leq 0$, we must also require $\dot{\gamma} \geq 0$ and $\dot{\gamma} y = 0$, together constituting the so-called Kuhn–Tucker conditions.

2.4. Numerical scheme and simulation setup

Simulating microstructures under large deformations requires a numerical scheme capable of handling the topological changes that the microstructures undergo. Due to mesh distortion issues, this makes the classical FEM not suitable for such simulations. DEM has successfully been used to study large deformation granular compaction. However, not all porous solids can be accurately approximated as granular as their microstructure is better described as a (semi-)continuous matrix of solid. Therefore, we perform numerical loading experiments of microstructures using the material point method (MPM). Similar to the finite element method (FEM), it is a numerical scheme to approximate solutions to the (weak forms of the) mass and momentum conservation equations of continuum mechanics. Dating back to Sulsky et al. [35], it can be considered an extension of particle-in-cell (PIC) methods, notably the fluid-implicit particle method (FLIP) [36]. It has since gained attention for being particularly suitable for large deformation modeling of solids. Although there exist several variations of MPM, we have resorted to symplectic time integration, a weighted PIC-FLIP combination for grid-particle interpolation [37] with quadratic B-spline interpolation function [38], as presented and used by, e.g., Klár et al. [33], Gaume et al. [34], Blatny et al. [17], Blatny et al. [39]. The full MPM algorithm used in this study is outlined in Appendix A.

A common challenge in elastoplastic modeling of strain-softening materials is the lack of uniqueness of solutions to the governing continuum equations, potentially leading to post-yield mesh-dependent results. As a remedy, rigorous regularizing techniques introduce a characteristic length scale in the governing equations, e.g., through higher-order gradient methods [40,41]. However, in microstructure-based modeling, this length scale is already given by the microstructural geometry, and such schemes are often not employed [18,42–45]. Nevertheless, we address the issue of mesh dependency by taking the mesh size into the plasticity criterion with the approach of Blatny et al.

[17] as this is a simple approach to mitigate the influence of the mesh in the numerical solution.

Uniaxial confined compression are performed on microstructures twice as long in the vertical direction as in the horizontal direction(s). A compressive plate on the top is imposed with a constant strain rate $\dot{\epsilon}$, with perfectly frictionless boundaries on all sides.[1] The volume-averaged Kirchhoff stress tensor $\langle\tau\rangle$ is computed, from which the volume-averaged mean stress $\langle p \rangle$ can be deduced. Moreover, both the plastic and elastic volumetric deformation of the microstructures' solid phase are computed. With the volume change factor of the solid phase defined as $J = \det(\boldsymbol{F}) = \det(\boldsymbol{F}^E)\det(\boldsymbol{F}^P) = J^E J^P$, this allows the investigation of the material's solid fraction evolution,

$$\phi(t) = \phi_0 \frac{J(t)}{1 - \dot{\epsilon}t} \tag{11}$$

accounting for both the elastic and plastic expansion and reduction of the solid phase volume of the microstructure, Here, ϕ_0 denotes the initial solid volume fraction at time $t = 0$.

In analogy with previous studies in soil and granular mechanics mentioned in the introduction, we investigate here the relation between inverse solid volume fraction $1/\phi$ as a function of the mean stress $\langle p \rangle$ in the microstructure. We will initially assume the solid phase has elastic and plastic parameters representative of ice with $E = 1$ GPa, $\nu = 0.3$, $c = 2.5$ MPa, $\varphi_f = 30°$, $\rho = 10^4$ kg/m^d and $\xi = 10^6$ such that the porous material can be considered as snow or firn.[2] The effect of different constitutive model parameters will be presented later in this article.

2.5. Representative volume element

In order to assess the minimum microstructure size which is representative of the macroscopic behavior, several simulations of various sizes were performed. Fig. 4 shows the result of such analysis for two-dimensional double-cut structures, where the quantity of interest is the fitted slope λ of the consolidation phase, $1/\phi \propto \lambda \cdot \log\langle p \rangle$ in the approximately linear region. For each size of the microstructure, measured in the number of mean wavelengths $\langle\omega\rangle$ per shortest side length l, seven stochastically identical structures were simulated. The analysis suggests a microstructure size of at least nine wavelengths, after which the mean slope fluctuates around a constant value and the deviations do not shrink significantly. This size is in agreement with previously reported

---

[1] Note the symbolic distinction between the Hencky strain ϵ on the microscale and the macroscopically imposed strain $\epsilon = Vt/l$, where V is the speed of the compressive plate and l is the side length of the microstructure.

[2] The density ρ was scaled by a factor 10 compared to the actual density of ice in order to speed up the computations which are limited by the elastic wave speed, knowing that this does not influence the response, similar to previous studies [17,46]. This will also be validated in Fig. 8d and Fig. 9d.
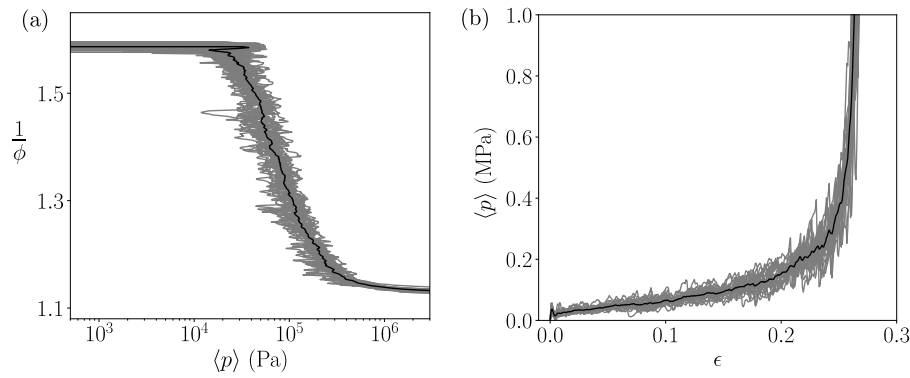
Fig. 5. Compression simulations of 24 random realizations of the microstructure from Fig. 1a (with $\phi_0 = 0.63$). The gray lines represent individual simulations while the black line is the mean response. In (a), the inverse solid area fraction $1/\phi$ is plotted against the mean stress $\langle p \rangle$, while in (b), the mean stress is plotted against the imposed compressive strain ϵ.
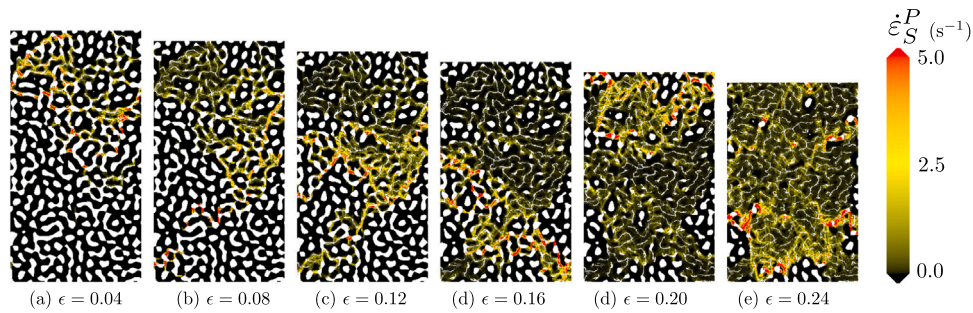

Fig. 6. Snapshots of the plastic Hencky strain rate $\dot{\varepsilon}_S^P$ in one of the microstructure from the compression simulations in Fig. 5 at different imposed compressive strains ϵ.
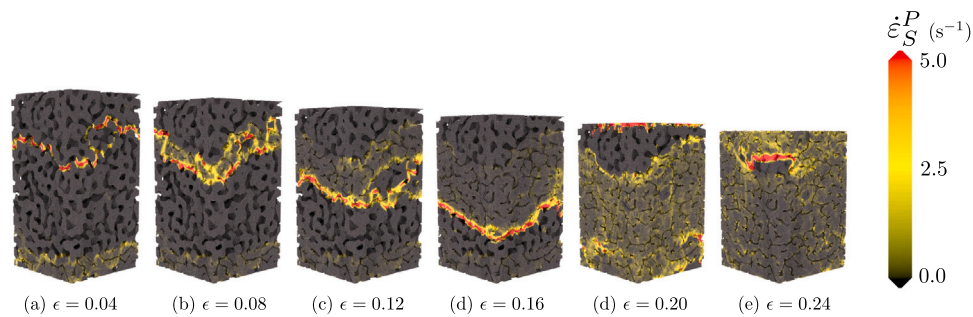

Fig. 7. Snapshots of the plastic Hencky strain rate $\dot{\varepsilon}_S^P$ in a three-dimensional equivalent microstructure of the two-dimensional microstructure presented in Fig. 6 under compression.

sizes for three-dimensional single-cut structures [17] and other previous findings [29,47] studying the convergence of the elastic modulus and failure strength with size.

3. Results

3.1. Demonstration

The GRF-MPM framework allows simulating the full deformation of microstructures that are geometrically different yet potentially having identical structural parameters. Fig. 5a shows the relation between the inverse solid fraction and mean stress from simulations of an ensemble of 24 stochastically identical isotropic ($a = 1$) and nearly-homogeneous ($b = 50$) two-dimensional microstructures with a solid fraction of $\phi = 0.63$ compressed with an imposed strain rate of $\dot{\epsilon} = 0.1 \text{ s}^{-1}$. Snapshots of an individual simulation/microstructure at different levels of compression are shown in Fig. 6. In addition, Fig. 7 presents the same snapshots for the equivalent three-dimensional structure. Colored in terms of the plastic strain rate, these snapshots highlight the evolution of the failure regions in the structure. From the

same set of simulations, Fig. 5b shows the mean stress as a function of imposed compressive strain. While individual simulations are associated with stress surges resulting in an erratic stress response, in the stochastic view the stress response can be considered to follow a mean path with certain upper and lower bounds on the fluctuations. These bounds, given by the "cloud" of the many simulations, permit a proper comparison of the mechanical response of samples with different structural properties.

3.2. Structures with high solid fraction

Figs. 8 and 9 show the evolution of the inverse solid fraction from a plethora of simulations, changing various properties of the microstructures as well as the imposed strain rate and dimensionality of the problem. Fig. 8 shows the result from a "dense" structure with $\phi_0 \approx 0.7$. In this case, it can be seen from Figs. 8a and b that the structures' level of heterogeneity and anisotropy, respectively, very weakly affect the consolidation response unless they are extremely anisotropic ($a \leq 0.4$). Specifically, there appears to be a slight trend of decreasing consolidation slope with both increasing heterogeneity
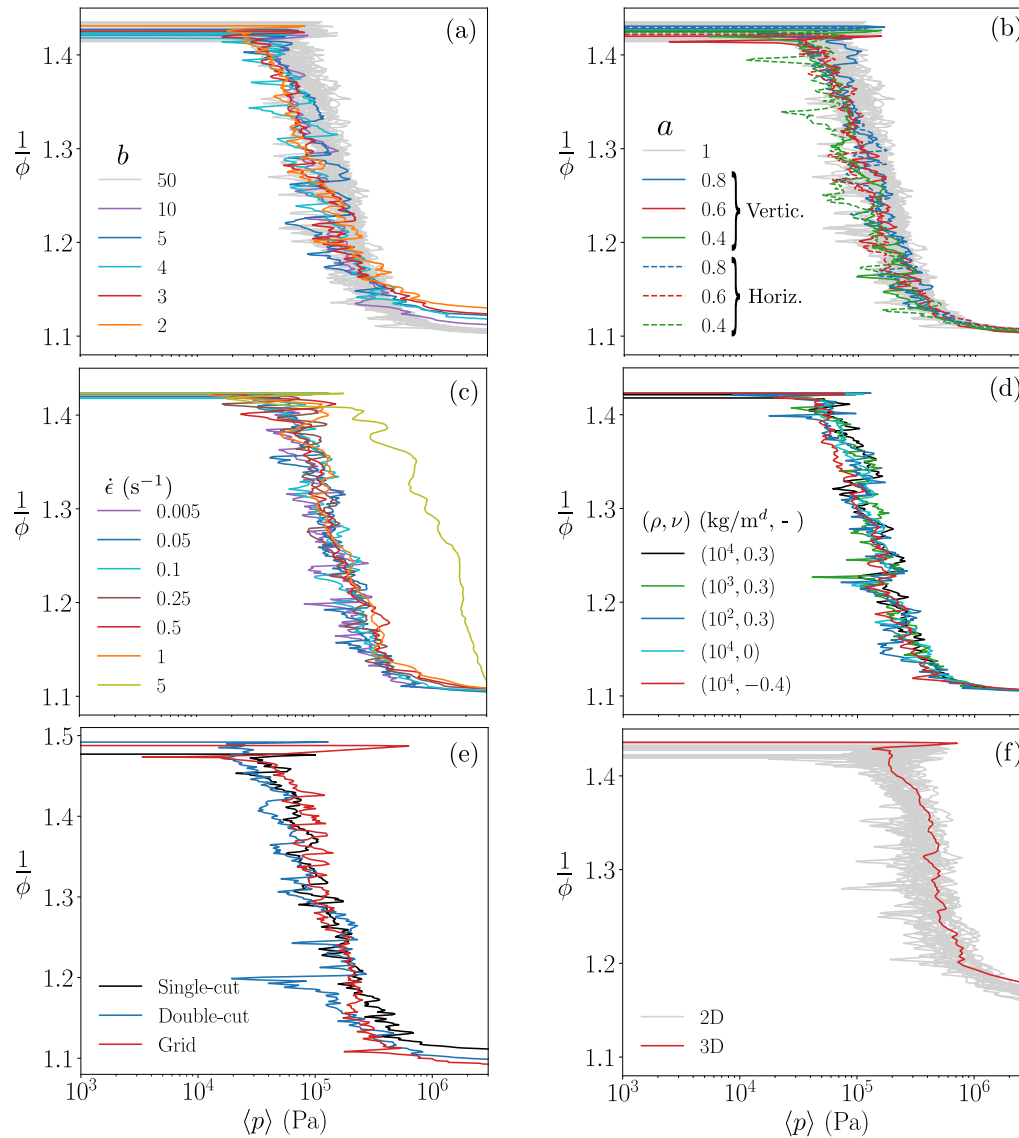
Fig. 8. Compression of single-cut two-dimensional GRF-structures of initial solid fraction $\phi_0 \approx 0.7$ with varying (a) the structures' heterogeneity, (b) the structures' anisotropy, (c) the imposed strain rate, (d) the solid phase density and Poisson's ratio. In (e), a single-cut, double-cut and grid-like structure are compared (note that here $\phi_0 = 0.67$ due to generation of comparable structures of same level of discretization). In (f), a two- and three-dimensional structure are compared, using $\gamma = 1.2$ such that the friction angle (Eq. (9)) with $d = 3$ is 30°. The "default" properties are those of an isotropic ($a = 1$) and nearly-homogeneous ($b = 50$) microstructure with $\dot{\epsilon} = 0.1$ s^{-1}, $\nu = 0.3$ and $\rho = 10^4$ kg/m^d.

and anisotropy. However, comparing to an ensemble of 20 stochastic isotropic and nearly-homogeneous structures (colored light gray in the plots), this is still within the error bounds. Moreover, the imposed strain rate (i.e., the velocity of the compressive top plate) has no impact unless it is so high that we create a propagation of a front of progressively compacted material, which is further analyzed in Appendix B. The consolidation curves for different imposed strain rates are plotted in Fig. 8c, which also indicate that stress fluctuations decrease with increasing plate speed. These stress fluctuations also tend to be suppressed with increasing sample width which averages out the erratic stress behavior, as seen in Fig. 4a. Furthermore, Fig. 8d shows that the density and Poisson's ratio of the solid phase do not influence the consolidation curve. The type of GRF-microstructure, whether single-cut or double-cut, does not affect the consolidation region, as shown in Fig. 8e. In this figure, the inverse solid fraction of a corresponding simulation of a grid-like structure (i.e., structure perforated with square holes as in Blatny et al. [39]) is also plotted, showing similar behavior. Finally, the dimensionality of the problem, i.e., whether we study microstructures in two or three spatial dimensions, does not affect the

consolidation region. This is presented in Fig. 8f, where the difference between the solid *volume* fraction in three spatial dimensions and solid *area* fraction in two spatial dimensions should be noted.

3.3. Structures with low solid fraction

The above conclusions about the (non-)influence of heterogeneity, anisotropy, solid phase density, solid phase Poisson's ratio and imposed strain rate remain valid also for lower solid fractions. This is shown in Fig. 9a–d for an initial solid fraction $\phi_0 \approx 0.35$. However, the particular type and dimensionality of the microstructure become relevant for the consolidation at low solid fractions. In Fig. 9e, it can be seen that a GRF-structure and grid-like structure do not provide an identical consolidation response when the initial solid fraction is low.

While in two spatial dimensions it is not possible to compare single-cut and double-cut structures for lower solid fractions due to the high percolation threshold for single-cut structures (at $\phi_0 \approx 0.5$), this is not a problem in three dimensions where percolation occurs at $\phi_0 \approx 0.15$. From such three-dimensional investigations, it was found that the
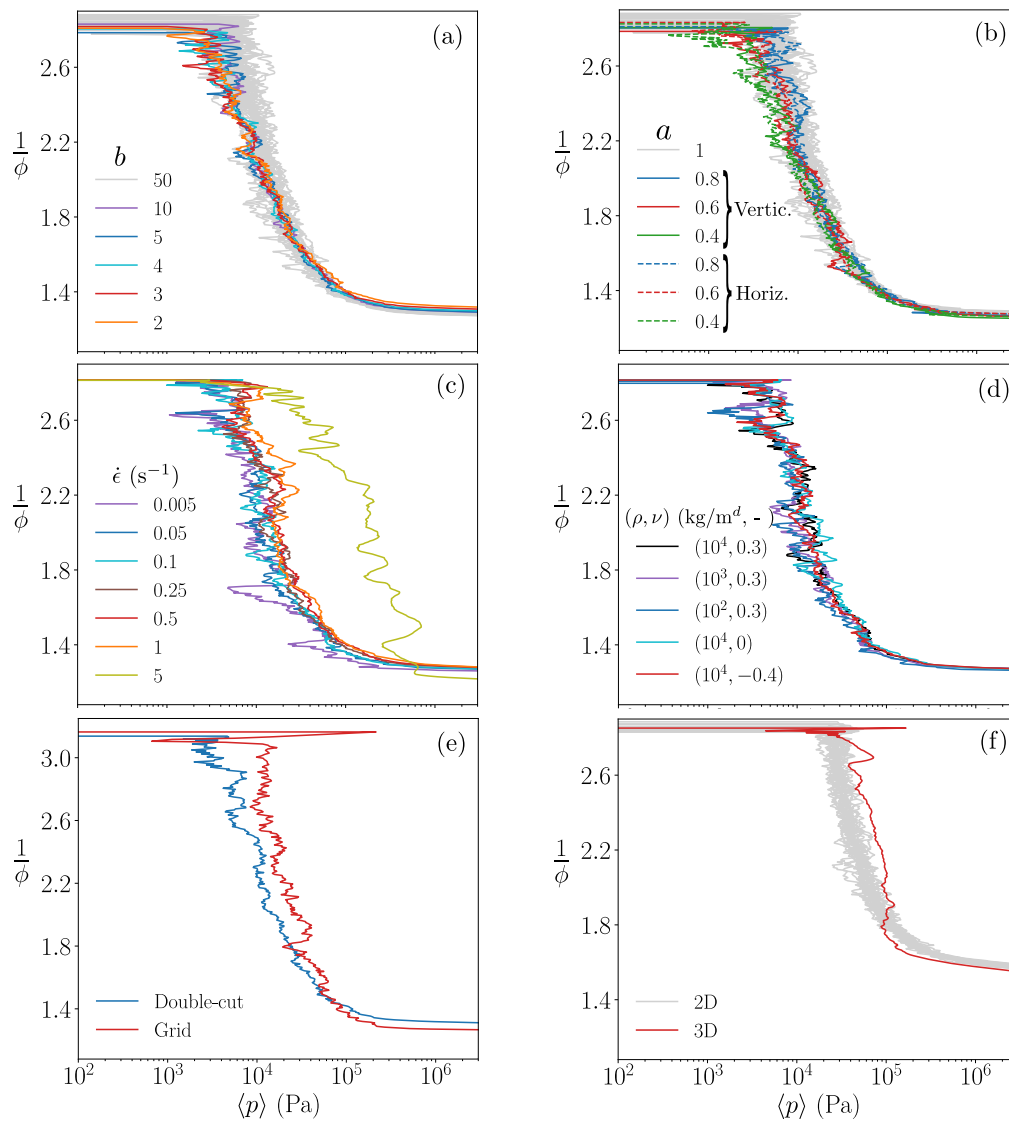
Fig. 9. Compression of double-cut two-dimensional GRF-structures of initial solid fraction $\phi_0 \approx 0.35$ with varying (a) the structures' heterogeneity, (b) the structures' anisotropy, (c) the imposed strain rate, (d) the solid phase density and Poisson's ratio. In (e), a double-cut and grid-like structure are compared (note that here $\phi_0 = 0.32$ due to generation of comparable structures of same level of discretization). In (f), a two- and three-dimensional structure are compared, using $\gamma = 1.2$ such that the friction angle (Eq. (9)) with $d = 3$ is 30°. The "default" properties are those of an isotropic ($a = 1$) and nearly-homogeneous ($b = 50$) microstructure with $\dot{\epsilon} = 0.1$ s^{-1}, $\nu = 0.3$ and $\rho = 10^4$ kg/m^d.

consolidation behavior is identical for $\phi_0 \gtrsim 0.5$. Comparing two- and three-dimensional double-cut structures, Fig. 9f suggests that the consolidation response is different when the solid fraction is low. In particular, $\phi_0 \approx 0.5$ is (again) the critical solid fraction above which the collapse becomes independent of the dimensionality.

This deviating response for low solid fractions can be related to how failure occurs on the microscale. While all structures display localization of strain in certain regions of the material, this localization appears more spatially scattered and temporally erratic in two-dimensional structures than in three-dimensional structures. In the latter case, unless the solid volume fraction is sufficiently large, the localization is not very erratic, and failure is mostly localized in one or more distinct compaction bands which to varying degree can propagate spatially within the sample. An increase in the initial solid volume fraction or a reduction of spatial dimension both imply a restriction of the possible movements of the individual strands of the microstructure. Such restrictions on the rearrangement possibilities increase the spatial extent of the failure zones. Thus, during the consolidation phase, the measured stress of a highly porous three-dimensional structure does not increase as much as the corresponding porous two-dimensional structure.

3.4. Universality in two-dimensional plastic consolidation

The end of the consolidation region, i.e., when the pores are closing, is marked by an exponential increase in the stress. While there is essentially no volume change due to *elastic* deformation during the consolidation, at the onset of densification there is a significant elastic volumetric compaction. Complete pore closure means $\phi = 1$, however, structures of smaller initial solid fraction reach densification at a smaller solid fraction than those with higher initial solid fraction, a result which is also observed for cellular materials in general [25]. This motivates the introduction of the solid fraction at densification, ϕ_d, defined as where the elastic deformation starts to significantly decrease the solid area/volume. In particular, it can be defined by a (rather insensitive) threshold on J^E falling below unity.

In compression simulations of two-dimensional periodic systems of discrete cohesive disks, Gilabert et al. [48] also considered compaction until densification and suggested a correction to the well-established linear relationship $1/\phi \propto \lambda \log(p)$ when reaching this large compaction. In particular, they suggested that the linear relationship with $\log(p)$ transitions to a linear relationship with $p^{-\alpha}$ where they report values
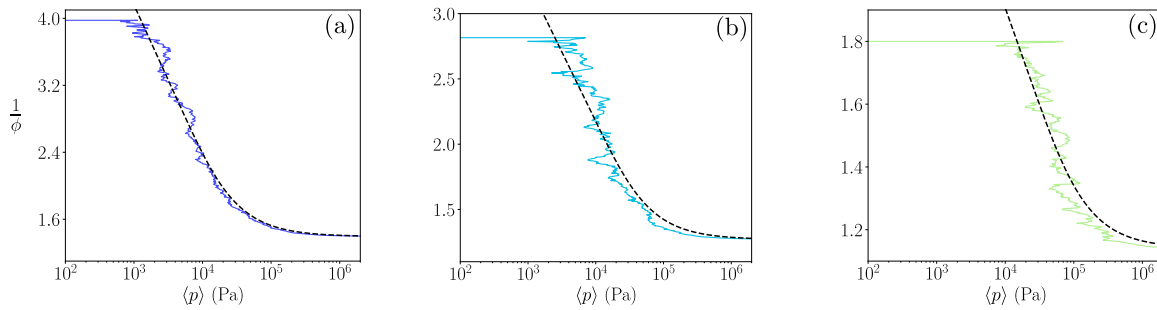
Fig. 10. The proposed relation of Gilabert et al. [48], Eq. (12), with λ fitted to the two-dimensional GRF-structures with (a) $\phi_0 = 0.25$ (giving $\lambda = 1.80$), (b) $\phi_0 = 0.35$ (giving $\lambda = 1.06$) and (c) $\phi_0 = 0.55$ (giving $\lambda = 0.62$). Note the data is colored similarly as in Fig. 11.
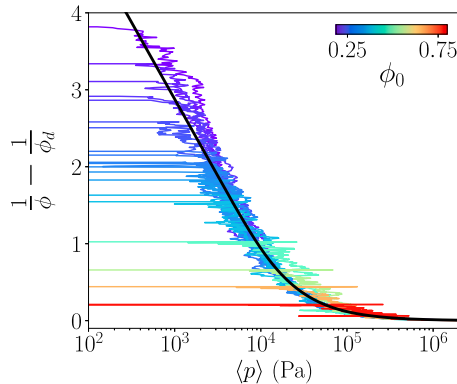

Fig. 11. Compression of two-dimensional GRF-structures of various initial solid volume fractions. The fit of Eq. (13) is included as the black solid line with $\lambda = 1.99$ and $p_d = 27.7$ kPa.

of α close to unity. Using $\alpha = 1$, their expression for the consolidation can be written

$$\frac{1}{\phi} = \frac{1}{\phi_0} - \lambda \log\left(\frac{p}{p_0}\left(1 - e^{-p_d/p}\right)\right) \tag{12}$$

where p_0 is the pressure at ϕ_0, and p_d is defined through $1/\phi_0 - 1/\phi_d = \lambda \log(p_d/p_0)$. Here, $\log$ denotes the base-10 logarithm. In Fig. 10, we fitted Eq. (12) to our data from two-dimensional structures of various initial solid fractions. With ϕ_d defined here as where $J^E < 0.995$, leaving λ the only fitting parameter, we obtain excellent fits with this function. We further note that in these fits λ decreases with ϕ_0.

Using the relation between p_0 and p_d, Eq. (12) can be written

$$\frac{1}{\phi} - \frac{1}{\phi_d} = \lambda \log\left(\frac{p_d/p}{1 - e^{-p_d/p}}\right) \tag{13}$$

Remarkably, when interpreting the pair (λ, p_d) as fitting parameters, we find that the consolidation data from all experiments of two-dimensional homogeneous and isotropic GRF-structures collapse on a curve described by Eq. (13). Fig. 11 illustrates this fit together with the simulation results, where the fit excludes the initial elastic and post-peak softening region for each simulation, yielding $\lambda = 1.99$ and $p_d = 27.7$ kPa. As mentioned earlier, there is a slight trend of a smaller consolidation slope for increasing heterogeneity and anisotropy. Sets of simulations performed for very heterogeneous structures ($b = 2$) and moderate level of anisotropy ($a = 0.6$) confirmed that, while leaving Eq. (13) an excellent fit, the fitted λ was found to be 1.55, thus lower than the one reported for homogeneous isotropic structures.

With the exception of Poisson's ratio (as seen in Figs. 8d and 9d), the consolidation curve does not remain invariant to the elastic modulus and plastic constitutive parameters on the solid phase (see Appendix C). This is because the stress at the onset of failure will be different when these parameters are changed. However, scaling for the stress at

failure, the consolidation curves remain similar across different values for Young's modulus E, cohesion c, friction γ and softening factor ξ. In the view of Eq. (13), these parameters only result in a shift of p_d, leaving λ a universal constant for the investigated microstructures across material parameters. In particular, p_d increases with c and γ and decreases with E and ξ. Further details on constitutive model/parameter dependencies are presented in Appendix C.

4. Discussion

It is instructive to compare the quantitative results of this study to that of similar studies from soil and granular mechanics. Using the linear relationship $1/\phi \propto \lambda \cdot \log(p)$, Wood [21] reports an index λ between roughly 0.2 and 1.2 for different soil types from around the world. From three-dimensional simulations of cohesive granular systems, Gaume et al. [16] finds $\lambda \approx 1.2$ when studying initial solid fractions ϕ_0 between 0.2 and 0.35. For ϕ_0 between 0.38 and 0.52, Gilabert et al. [48] reports λ between 0.45 and 0.8. These values are smaller than, but close to, the values we obtained in this region with isotropic structures. However, with increasing heterogeneity and anisotropy we also witnessed a smaller λ. Using the linear relationship, Poquillon et al. [23] proposes, based on compaction experiments of iron powders with ϕ_0 below 0.2, an expression for λ that depends on ϕ_0 and yield pressure. In particular, they report a decreasing λ with increasing ϕ_0. This is consistent with our results as reported in Fig. 10. We finally note that our fit and corresponding plastic index λ were a result of data from a larger range of initial porosities (ϕ_0 between 0.25 and 0.75) than in any of these previous studies.

Moreover, similar to the idealized granular sphere system study by Gaume et al. [16], we found no influence of the cohesion on the consolidation slope. In their study, the spheres were connected by bonds which could not heal after breakage, analogous to the brittle assumption of the solid phase in our study. This is in contrast to the experiments of Castellanos [24] on toners having attractive inter-grain forces. In particular, assuming the attraction arises from van der Waals forces, they found a power law of λ with the granular Bond number. This number gives the ratio between the inter-grain attractive force and grain mass.

In the more porous three-dimensional structures (Fig. 9f), the stress does not display the gradual increase observed in the other structures. This is similar to the constant stress plateau observed in highly porous elastic-brittle cellular solids ($\phi < 0.3$) [25]. The absence of a stress plateau in two-dimensional structures is related to the absence of a compaction band, which we attributed to different type of deformation mechanism on the microscale. The (dynamic) compaction bands emerging in our numerical three-dimensional simulations have been observed experimentally in snow [49,50], porous rocks [51] and granular packs [52,53], and their occurrence generally depend on the bulk material properties and strain rate [39].

While the numerical experiments presented in this study did not expose a significant difference of the consolidation response depending on the degree of anisotropy, the anisotropy did affect the (small

strain) yield strength. In particular, the more horizontally aligned the structure is, the smaller the yield stress. This observation is consistent with Mangipudi and Onck [11] where a finite element beam network was employed to simulate cellular solids. Studying the effect of anisotropy on large deformation of polyurethane foam, Tu et al. [54] performed experimental compression tests that unveiled different plastic consolidation responses. For vertically aligned structures, they observed post-yielding compaction bands propagating down the structure at constant stress level until densification. On the other hand, for horizontally aligned structures, they observed uniformly distributed deformation causing a linearly increasing stress between yield and densification. This is reminiscent of the difference between highly porous two- and three-dimensional structures presented in Fig. 9f and as discussed in the previous paragraph. The difference in deformation mechanism due to degree of anisotropy could be a result of their polyurethane foam being much more porous than studied in this work. In the GRF-MPM framework of this article, lower solid fractions cannot currently be studied due to the extremely fine discretization needed for such structures (and single-cut structures cannot be used due to lack of percolation). Nevertheless, our results are consistent with Tu et al. [54] in that the same type of deformation mode on the microscale causes the same (increasing) stress evolution until densification.

We have not introduced any specific self-contact treatment in the MPM scheme, implying that these events are automatically handled through the interpolation to the background grid. To be more specific, each particle has a local support, influencing grid nodes within a certain distance. As such, when particles belonging to different microstructural grains approach each other, the grid nodes located around the contact area will be assigned velocities that are a weighted average of velocities of all nearby particles. Effectively, this means that when these particles are brought together, they become a part of the same continuum and will interact with each other as dictated by the constitutive model, in particular through the internal friction angle given by the Drucker–Prager model. In a material like snow, this may be a decent assumption as the constituting ice grains of the snow microstructure will, when brought to contact, sinter together and become one grain (unless of course the strain rate is too high for sintering to occur) [55–57]. In many other materials, this assumption may not adequately represent reality as the friction between two microstructural grains may be different from the internal friction angle. However, the good agreement observed with previous studies, in particular that of Gilabert et al. [48], suggests that the assumption is acceptable for our purposes. In the literature, different ways of treating self-contact in MPM have been proposed, which all come with certain computational costs. In particular, contacts can be treated by attributing a background grid for each individual material object and then applying a Coulomb friction law on the nodal velocities when the objects come into contact [58]. In our case, this means that different microstructural grains must be distinguished a priori, which is not trivial as they inherently belong to the same continuum. Moreover, neighboring grains should not be considered having a frictional contact unless they have fractured and been brought to contact again. Along these lines, Homel and Herbold [59] suggested using an evolving scalar damage field in a way that allows dynamical partitioning of the material into contact pairs along fracture surfaces.

As the main focus of this work has been the microstructures' morphological influence on the mechanical results, we chose the Drucker–Prager yield criterion of Eq. (8) as we argued it was the simplest model offering three properties of porous brittle geomaterials as outlined in Section 2.3. These three properties were pressure-dependency, strong post-failure softening and asymmetry in tensile/compressive strength. Modeling different materials requires, in addition to adapting the microstructural morphological parameters, the appropriate choice of elastic (E, ν) and plastic (c, γ, ξ) parameters. For certain materials, the Drucker–Prager yield criterion could be extended to include a compressive cap, this being particularly relevant for rocks/sandstone in order to

account for crushing by introducing a hardening cap at high pressures. However, for many other porous materials, the solid phase material may not be adequately described by a Drucker–Prager-like model at all, and may also display rate- and/or temperature-dependency which were not included in this study. Therefore, the results presented here cannot be claimed valid for materials whose solid phase is behaves differently from this study's assumptions. Nevertheless, the presented framework is adaptable to include any constitutive model for the solid phase (Appendix C). Moreover, we have only studied porous structures which do not contain a secondary phase (air, water, etc.) in the pores. Future work could, for example, try to simulate air/water in the voids with an equation of state. However, this also raises the question of the connectivity of the voids (e.g., in Fig. 1 we see the voids are closed), and potentially how the secondary phase may be able to drain.

With increasing progress in additive manufacturing of materials, artificial structures can be produced where one can control morphology and solid phase properties, potentially allowing physical experiments in the same parameter space as our numerical study. In particular, Shenhav and Sherman [60] conducted compression experiments on 3D-printed porous brittle structures to study fracture mechanisms. However, their study was limited to idealized grid-like geometries and did not consider very large deformations. Focusing on the large plastic deformations, Zhang et al. [61] reviews the plastic collapse in additively manufactured auxetic porous structures with idealized unit cells. In the future, 3D-printing GRF microstructures with brittle plastics may allow for physical experiments to support the numerical observations presented here.

5. Concluding remarks

Relying on a set of artificially generated stochastic microstructures, this study has investigated the dependence of the microstructure on the macroscopic plastic consolidation response of porous brittle solids. Limited to structures whose bulk material is represented by a Drucker–Prager yield criterion and with initial solid fractions $\phi_0 \in [0.25, 0.75]$, the results of the numerical experiments presented in this article have shown that the solid fraction is the main relevant quantity that governs the consolidation of the structures. In particular, while heterogeneity and anisotropy in general only weakly influence the plastic consolidation, for $\phi_0 \lesssim 0.5$ the structural geometry and dimensionality of the problem become relevant. This is a result of different failure mechanisms on the microscale. Furthermore, this study has revealed that the plastic consolidation in two-dimensional structures can be described by a universal function and plasticity index similar to that proposed for systems of discrete cohesive disks. The presented framework could be adapted to study porous materials whose solid phase is rate- and/or temperature-dependent, and additionally enhanced to simulate voids containing a secondary phase such as air or water. While the stochastic-numerical experiments of this work allowed several conclusions about porous brittle solids to be made, further investigations can become excessively time-consuming, especially for three-dimensional structures, structures of very low solid fraction and when a sufficiently large stochastic ensemble is required. With increasing computational power in the future, the approach presented here can provide further and more detailed insight into the mechanics of any porous solid with continuous microstructures.

Declaration of competing interest

The authors declare that they have no known competing financial interests or personal relationships that could have appeared to influence the work reported in this paper.
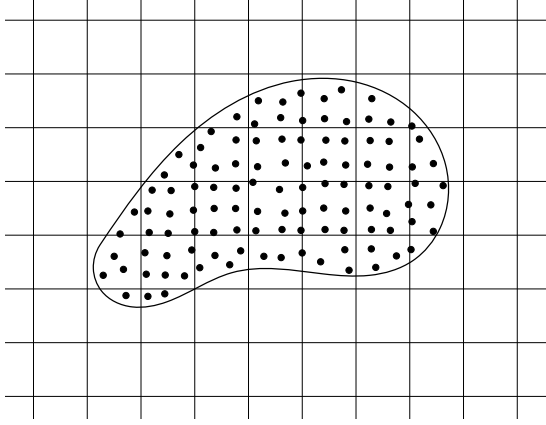
Acknowledgments

Fig. A.12. MPM discretization. A material domain discretized by particles on a background regular grid. Note that the material boundary is not modeled explicitly and only drawn here with a solid curved line in order to highlight the material domain.
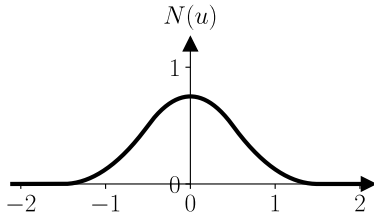

Fig. A.13. The quadratic B-spline of Eq. (A.2).

Appendix A. The MPM algorithm

Algorithm 1 (adapted from [17,39]) outlines the steps of the MPM scheme to approximate solutions to the (weak form of the) momentum conservation equation. The microstructures' solid phase is discretized into N_p of material particles with constant and equal mass m_p, initially equal volume V_p and initially zero velocity v_p. A fixed Eulerian grid with uniform grid spacing Δx is used, as illustrated in Fig. A.12. We employ interpolation functions $N_i(x_p)$ between a grid node i and a particle at a coordinate x_p on the form

$$N_i(x_p) = N\left(\frac{x_p - x_i}{\Delta x}\right) N\left(\frac{y_p - y_i}{\Delta x}\right) N\left(\frac{z_p - z_i}{\Delta x}\right) \quad \text{(A.1)}$$

with $N(\cdot)$ given by the quadratic B-spline

$$N(u) = \begin{cases} \frac{3}{4} - |u|^2, & \text{if } |u| < \frac{1}{2} \\ \frac{1}{2}(\frac{3}{2} - |u|)^2, & \text{if } \frac{1}{2} \leq |u| < \frac{3}{2} \\ 0, & \text{otherwise} \end{cases} \quad \text{(A.2)}$$

as plotted in Fig. A.13. Note that mass is automatically conserved as the total mass is the sum of particle masses which individually remain constant in time.

The algorithm relies on an *elastic predictor–plastic corrector scheme* following Simo [62], where, for each time step, it is initially assumed the deformation is elastic and later corrected if the step resulted in a non-admissible state outside the yield surface. We call the stress (or strain) state of the initial elastic prediction the *trial* state. A plastic flow

rule dictates how the correction occurs, in other words, how the trial state should be projected back to the yield surface. With the plastic rate of deformation given by Eq. (10), we have[3]

$$l^P = \dot{\gamma}\frac{\text{dev}(\tau)}{\|\text{dev}(\tau)\|} = \dot{\gamma}\frac{\text{dev}(\varepsilon)}{\|\text{dev}(\varepsilon)\|} \quad \text{(A.3)}$$

where we in the last equality made use of the elastic law and using the notation $\|A\| = \sqrt{A : A}$. This choice induces no plastic compaction/dilatancy. The Drucker–Prager yield surface is a cone in principle stress space, and trial states with p smaller than that of the cone's tip must be treated exceptionally. In particular, for these states, i.e., with $p < -ce^{-\xi\varepsilon_S^P}$, we make the natural choice of projecting them to the closest point on the yield surface, which is the state at the tip of the Drucker–Prager cone. However, this last choice will induce a plastic dilatancy. An illustration of the flow rule is sketched in Fig. A.14. While the (small) plastic dilatancy induced by the flow rule may not necessarily represent issue in the microstructural compression simulations, we would like to minimize this effect by using the plastic volume correction technique by Pradhana [63]. As this very simple and straightforward technique may not yet be familiar in the community, we briefly outline it here: We track the plastic volumetric expansion $\varepsilon_V^{P,n+1} = \varepsilon_V^{P,n} + \text{tr}(\varepsilon^{\text{trial}}) - \text{tr}(\varepsilon^{n+1})$, which is initially zero. This is then used to artificially shift the location of the cone's tip such that the projection in Step 11 in Algorithm 1 can instead be written

$$\varepsilon_p^{E,n+1} = \begin{cases} \varepsilon_p^{E,\text{trial}} - \Delta\gamma_p\frac{\text{dev}(\varepsilon_p^{E,\text{trial}})}{\|\text{dev}(\varepsilon_p^{E,\text{trial}})\|} + \frac{1}{d}\varepsilon_{V,p}^{P,n}I, & \text{if } p_p^{\text{trial}} \geq -ce^{-\xi\varepsilon_{S,p}^P} \\ \frac{c}{Kd}e^{-\xi\varepsilon_{S,p}^P}, & \text{otherwise} \end{cases}$$

where the variable ε_V^P must be reset to zero once a particle is not in a dilating state.

In MPM, the way in which information is transferred between grid nodes and particles significantly affects the overall dissipation of the numerical scheme. No transfer is completely loss-free, and with these transfers happening for every time step, this could add up to a notable dissipation. As seen in Step 13 of the Algorithm 1, a weighted combination of the particle-in-cell (PIC) and fluid-implicit-particle (FLIP) schemes provides a trade-off between the amount of numerical dissipation and stability of the scheme [37]. While we have used a weighting parameter $\alpha = 0.99$ in order to introduce minimal dissipation, a sensitivity study on this parameter reveals it does not significantly influence the plastic consolidation phase. This is presented in Fig. A.15, where we observe that even for a rather small value $\alpha = 0.8$, we are within the scatter of fluctuations, and the plastic consolidation is comparable to that of $\alpha = 0.99$. We note there exist other transfer schemes, e.g., Affine PIC [64,65] which preserves angular momentum exactly, or perhaps even better, Polynomial PIC [66] or Power PIC [67] which were developed very recently and can reduce the amount of dissipation further.

We refer to the time integration as symplectic since the positions are updated based on the current velocities, see Step 14 in Algorithm 1. It should be emphasized that this is not an implicit time integration scheme, no linear systems of equations are solved (no consistent tangent stiffness is derived), and the time step Δt is bound by the Courant–Friedrichs–Lewy (CFL) condition. In particular, we allow for adaptive time stepping by adhering to the CFL condition while at the same time ensuring that elastic waves do not travel more than Δx within the time Δt. This is described in Step 1, where we used the constants $C_{\text{CFL}} = 0.6$ and $C_{\text{el}} = 0.5$.

---

[3] Note that since the plastic multiplier $\dot{\gamma}$ is arbitrary we absorbed other constants into it.
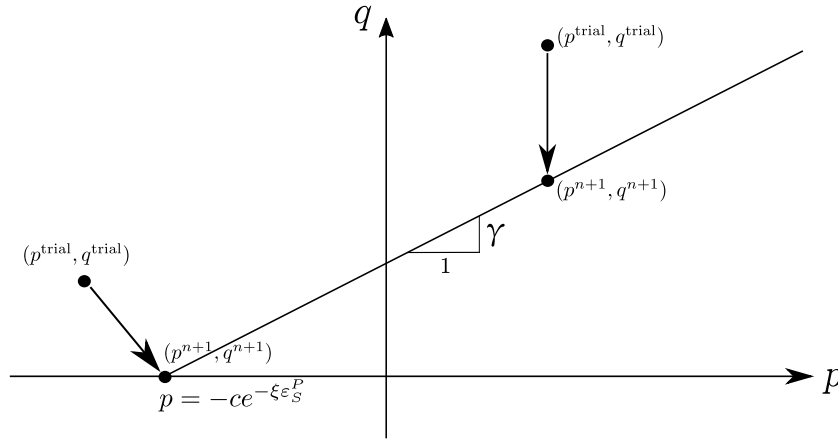
Fig. A.14. Flow rule. Two example trial states are projected to the yield surface, here illustrated in the space of p and q.
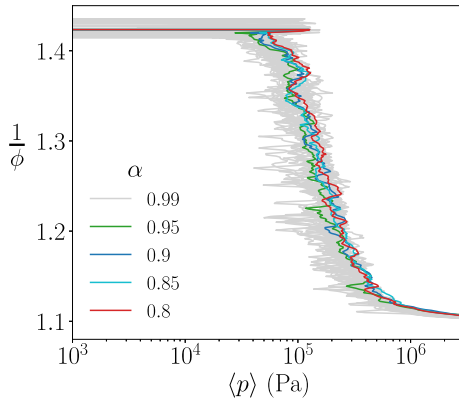

Fig. A.15. Influence of the FLIP-PIC ratio α on the plastic collapse of the two-dimensional isotropic single-cut microstructure with $\phi = 0.7$ used in Fig. 9 with $\alpha = 0.99$.

Appendix B. Effect of imposed strain rate

The deformation manifests itself differently on the microscale depending on the imposed strain rate. At low strain rates, below $\dot{\epsilon} = 5\ \mathrm{s}^{-1}$, the microscopic deformation is erratically scattered throughout the structure. At higher strain rates, a structure-spanning zone of high plastic compaction nucleates at the top and causes propagation of a front of progressively compacted material. The propagation continues until the bottom of the structure. Such type of compaction has been observed in porous rocks and steel foams [68–70]. The two types of compaction for low and high imposed strain rates are shown in Fig. B.16 within a dense microstructure and in Fig. B.17 within a more porous structure. Our finding of a critical strain rate above which these dynamic compaction patterns appear is in line with the study of Blatny et al. [39] who, using idealized two-dimensional structures with a perfectly-plastic von Mises solid phase, found that the deformation pattern transitions from spatially erratic to propagating compaction bands at a material-dependent critical strain rate.

Appendix C. Effect of solid phase constitutive model

The effect of changing the plastic constitutive Drucker–Prager parameters on the solid phase on the consolidation response is shown in Fig. C.18. The effect is equal to a shift of the stress at onset of failure, leaving the consolidation response remains similar. Changing Young's modulus will have an analogous effect as this will also change the stress at failure.

Algorithm 1: Elastoplastic symplectic Euler B-spline PIC-FLIP MPM

initialize $m_p, V_p, \boldsymbol{x}_p, \boldsymbol{v}_p = \boldsymbol{0}$, $\boldsymbol{F}^E = \boldsymbol{I}$, $\varepsilon^P_{S,p} = 0$

for $n \leftarrow 0$ **to** *max time steps* **do**

1. adapt time step: $\Delta t = \min\left(C_{\mathrm{CFL}} \frac{\Delta x}{\max_p |\boldsymbol{v}^n_p|},\ C_{\mathrm{el}} \frac{\Delta x}{\sqrt{E/\rho}} \right)$

2. interpolate grid mass: $m^n_i = \sum\limits_{p=1}^{N_p} m_p N_i(\boldsymbol{x}^n_p)$

3. interpolate grid velocity: $\boldsymbol{v}^n_i = \frac{1}{m^n_i} \sum\limits_{p=1}^{N_p} m_p \boldsymbol{v}^n_p N_i(\boldsymbol{x}^n_p)$

4. get grid force: $\boldsymbol{f}^n_i = -\sum\limits_{p=1}^{N_p} V^0_p \boldsymbol{\tau}(\boldsymbol{F}^{E,n}_p) \nabla N_i(\boldsymbol{x}^n_p)$

5. update grid velocity: $\boldsymbol{v}^{n+1}_i = \boldsymbol{v}^n_i + \frac{\Delta t}{m^n_i} \boldsymbol{f}^n_i$

6. apply boundary conditions: $\boldsymbol{v}^\perp_{i \in \partial\Omega} = 0$

7. get trial elastic deformation gradient on the particles:
   $$\boldsymbol{F}^{E,\mathrm{trial}}_p = \left(\boldsymbol{I} + \Delta t \sum_{i \in \mathrm{grid}} \boldsymbol{v}^{n+1}_i \left(\nabla N_i(\boldsymbol{x}^n_p) \right)^T \right) \boldsymbol{F}^{E,n}_p$$

8. perform SVD of $\boldsymbol{F}^{E,\mathrm{trial}}_p = \boldsymbol{U}^E_p \boldsymbol{\Sigma}^{E,\mathrm{trial}}_p (\boldsymbol{V}^E_p)^T$

9. get trial elastic Hencky strain: $\boldsymbol{\varepsilon}^{E,\mathrm{trial}}_p = \ln \boldsymbol{\Sigma}^{E,\mathrm{trial}}_p$

10. check yield criterion $y(p^{\mathrm{trial}}_p, q^{\mathrm{trial}}_p)$ where
    $p^{\mathrm{trial}}_p = -K\,\mathrm{tr}(\boldsymbol{\varepsilon}^{E,\mathrm{trial}}_p)$ and $q^{\mathrm{trial}}_p = \sqrt{6G}||\mathrm{dev}(\boldsymbol{\varepsilon}^{E,\mathrm{trial}}_p)||$.
    If $y \leq 0$, then $\boldsymbol{\varepsilon}^{E,n+1}_p = \boldsymbol{\varepsilon}^{E,\mathrm{trial}}_p$ and proceed to step 12

11. obtain the new strain state by projecting the trial state back to the yield surface according to the non-associative flow
    rule, $\boldsymbol{\varepsilon}^{E,n+1}_p = \begin{cases} \boldsymbol{\varepsilon}^{E,\mathrm{trial}}_p - \Delta\gamma_p \frac{\mathrm{dev}(\boldsymbol{\varepsilon}^{E,\mathrm{trial}}_p)}{||\mathrm{dev}(\boldsymbol{\varepsilon}^{E,\mathrm{trial}}_p)||}, & \text{if } p^{\mathrm{trial}}_p \geq -ce^{-\xi\varepsilon^P_{S,p}} \\ \frac{c}{Kd} e^{-\xi\varepsilon^P_{S,p}}, & \text{otherwise} \end{cases}$
    and update the softening variable
    $\varepsilon^P_{S,p} = \varepsilon^P_{S,p} + \left(||\mathrm{dev}(\boldsymbol{\varepsilon}^{E,\mathrm{trial}}_p)|| - ||\mathrm{dev}(\boldsymbol{\varepsilon}^{E,n+1}_p)|| \right)$

12. update elastic deformation gradient on the particles
    $\boldsymbol{F}^{E,n+1}_p = \boldsymbol{U}^E_p e^{\boldsymbol{\varepsilon}^{E,n+1}_p} (\boldsymbol{V}^E_p)^T$

13. update particle velocity: $\boldsymbol{v}^{n+1}_p = \alpha \boldsymbol{v}^{\mathrm{FLIP}}_p + (1-\alpha)\boldsymbol{v}^{\mathrm{PIC}}_p$ where
    $\boldsymbol{v}^{\mathrm{PIC}}_p = \sum\limits_{i \in \mathrm{grid}} \boldsymbol{v}^{n+1}_i N_i(\boldsymbol{x}^n_p), \quad \boldsymbol{v}^{\mathrm{FLIP}}_p = \boldsymbol{v}^n_p + \sum\limits_{i \in \mathrm{grid}} (\boldsymbol{v}^{n+1}_i - \boldsymbol{v}^n_i) N_i(\boldsymbol{x}^n_p)$

14. update positions: $\boldsymbol{x}^{n+1}_p = \boldsymbol{x}^n_p + \Delta t\,\boldsymbol{v}^{\mathrm{PIC}}_p$
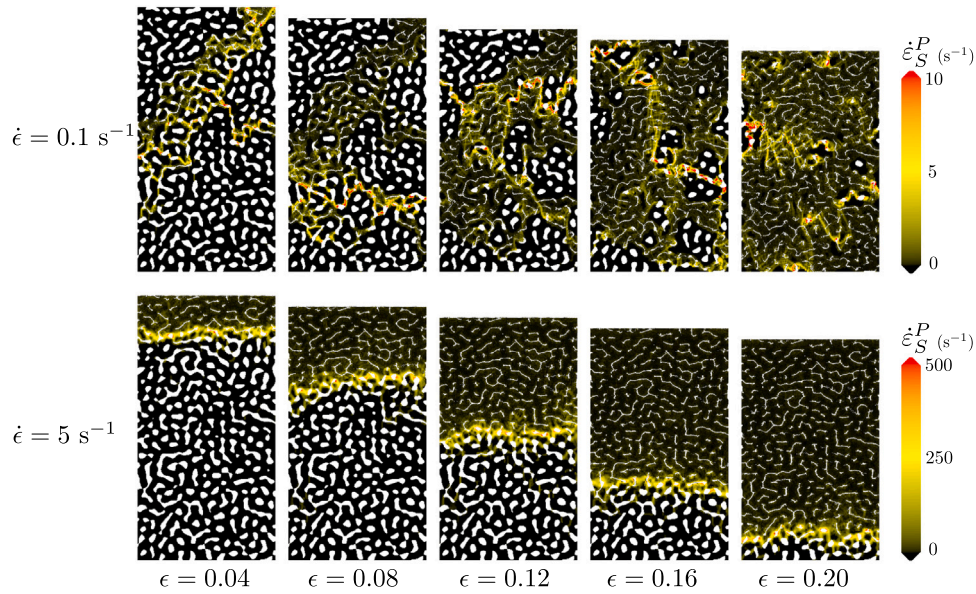
end

Fig. B.16. Plastic strain rate $\dot{\varepsilon}_S^P$ visualized in the microstructure of Fig. 8c under slow (upper row) and fast (lower row) imposed compressive strain rate $\dot{\epsilon}$.
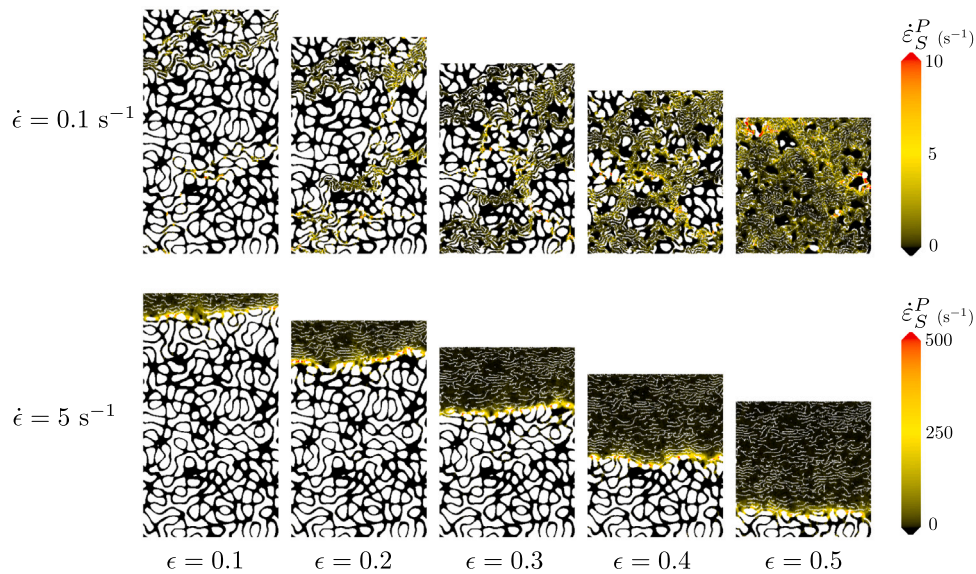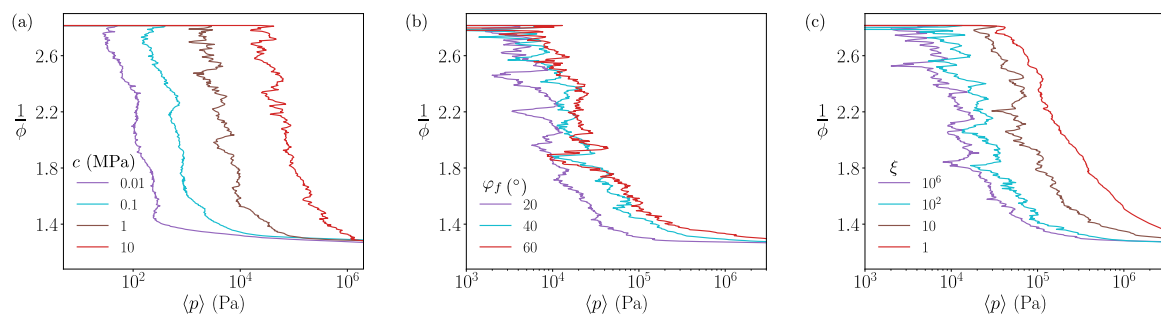

Fig. B.17. Plastic strain rate $\dot{\varepsilon}_S^P$ visualized in the microstructure of Fig. 9c under slow (upper row) and fast (lower row) imposed compressive strain rate $\dot{\epsilon}$.

Fig. C.18. Effect of plastic constitutive parameters of the Drucker–Prager model, in particular the (a) cohesion c, (b) friction angle φ_f and (c) softening factor ξ. Here, a double-cut structure of $\phi_0 = 0.35$ was used.
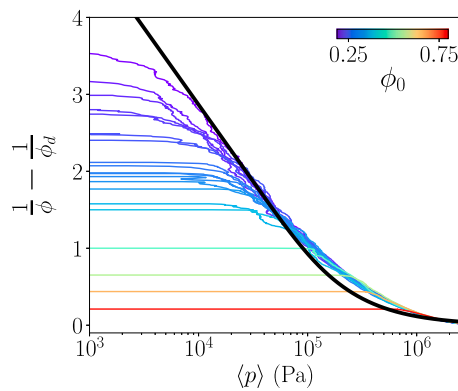
Fig. C.19. Same as Fig. 11 except here a perfectly-plastic von Mises constitutive model was used for the solid phase of the microstructure. The black line is Eq. (13) with $\lambda = 1.99$ (as in Fig. 11) and $p_d = 273$ kPa.

Interestingly, changing the constitutive solid phase model to a perfectly-plastic von Mises model, still leaves Eq. (13) a decent fit. This is illustrated in Fig. C.19, using the same λ as found for the Drucker–Prager strain-softening model, only a shift of p_d is used in the fit. The von Mises yield criterion is given by $y(q) = q - q_m$ where q_m is a chosen "shear strength" constant. Here, the value of q_m was chosen to match the Drucker–Prager yield criterion of Eq. (8) at vanishing mean stress.

References

[1] H.W. Green, T.E. Young, D. Walker, C.H. Scholz, Anticrack-associated faulting at very high pressure in natural olivine, Nature 348 (1990) 720–722, http://dx.doi.org/10.1038/348720a0.

[2] J. Heierli, P. Gumbsch, M. Zaiser, Anticrack nucleation as triggering mechanism for snow slab avalanches, Science 321 (2008) 240–243, http://dx.doi.org/10.1126/science.1153948.

[3] S.J. Hollister, Porous scaffold design for tissue engineering, Nature Mater. 4 (2005) 518–524, http://dx.doi.org/10.1038/nmat1421.

[4] A.G. Slater, A.I. Cooper, Function-led design of new porous materials, Science 348 (2015) aaa8075, http://dx.doi.org/10.1126/science.aaa8075.

[5] W.T. George, D. Vashishth, Damage mechanisms and failure modes of cortical bone under components of physiological loading, J. Orthop. Res. 23 (2005) 1047–1053, http://dx.doi.org/10.1016/j.orthres.2005.02.008.

[6] Z. Hashin, S. Shtrikman, A variational approach to the theory of the elastic behaviour of multiphase materials, J. Mech. Phys. Solids 11 (1963) 127–140, http://dx.doi.org/10.1016/0022-5096(63)90060-7.

[7] A.L. Gurson, Continuum theory of ductile rupture by void nucleation and growth: Part I—Yield criteria and flow rules for porous ductile media, J. Eng. Mater. Technol. 99 (1977) 2–15, http://dx.doi.org/10.2172/7351470.

[8] I.J. Gibson, M.F. Ashby, The mechanics of three-dimensional cellular materials, Proc. R. Soc. Lond. Ser. A Math. Phys. Eng. Sci. 382 (1982) 43–59, http://dx.doi.org/10.1098/rspa.1982.0088.

[9] P.P. Castañeda, The effective mechanical properties of nonlinear isotropic composites, J. Mech. Phys. Solids 39 (1991) 45–71, http://dx.doi.org/10.1016/0022-5096(91)90030-R.

[10] C. Petit, S. Meille, E. Maire, Cellular solids studied by x-ray tomography and finite element modeling – a review, J. Mater. Res. 28 (2013) 2191–2201, http://dx.doi.org/10.1557/jmr.2013.97.

[11] K. Mangipudi, P. Onck, Multiscale modelling of damage and failure in two-dimensional metallic foams, J. Mech. Phys. Solids 59 (2011) 1437–1461, http://dx.doi.org/10.1016/j.jmps.2011.02.008.

[12] F. Fritzen, S. Forest, T. Böhlke, D. Kondo, T. Kanit, Computational homogenization of elasto-plastic porous metals, Int. J. Plast. 29 (2012) 102–119, http://dx.doi.org/10.1016/j.ijplas.2011.08.005.

[13] M.-T. Hsieh, B. Endo, Y. Zhang, J. Bauer, L. Valdevit, The mechanical response of cellular materials with spinodal topologies, J. Mech. Phys. Solids 125 (2019) 401–419, http://dx.doi.org/10.1016/j.jmps.2019.01.002.

[14] E. Garboczi, A. Day, An algorithm for computing the effective linear elastic properties of heterogeneous materials: Three-dimensional results for composites with equal phase Poisson ratios, J. Mech. Phys. Solids 43 (1995) 1349–1362, http://dx.doi.org/10.1016/0022-5096(95)00050-S.

[15] P. Hagenmuller, G. Chambon, M. Naaim, Microstructure-based modeling of snow mechanics: a discrete element approach, Cryosphere 9 (2015) 1969–1982, http://dx.doi.org/10.5194/tc-9-1969-2015.

[16] J. Gaume, H. Löwe, S. Tan, L. Tsang, Scaling laws for the mechanics of loose and cohesive granular materials based on Baxter's sticky hard spheres, Phys. Rev. E 96 (2017) 032914, http://dx.doi.org/10.1103/PhysRevE.96.032914.

[17] L. Blatny, H. Löwe, J. Gaume, Computational micromechanics of porous brittle solids, Comput. Geotech. 140 (2021) 104284, http://dx.doi.org/10.1016/j.compgeo.2021.104284.

[18] N. Guo, J. Zhao, A coupled FEM/DEM approach for hierarchical multiscale modelling of granular media, Internat. J. Numer. Methods Engrg. 99 (2014) 789–818, http://dx.doi.org/10.1002/nme.4702.

[19] J. Desrues, T.K. Nguyen, A. Argilaga, S. Dal Pont, G. Combe, D. Caillerie, Double scale numerical FEM-DEM analysis for cohesive-frictional materials, in: 10th Euroconference on Rock Physics and Rock Mechanics, Aussois, France, 2014.

[20] A.N. Schofield, P. Wroth, Critical State Soil Mechanics, McGraw-Hill London, 1968.

[21] D.M. Wood, Soil Behaviour and Critical State Soil Mechanics, Cambridge University Press, 1991, http://dx.doi.org/10.1017/CBO9781139878272.

[22] E.E. Walker, The properties of powders. part vi. the compressibility of powders, Trans. Faraday Soc. 19 (1923) 73–82, http://dx.doi.org/10.1039/TF9231900073.

[23] D. Poquillon, J. Lemaitre, V. Baco-Carles, P. Tailhades, J. Lacaze, Cold compaction of iron powders—relations between powder morphology and mechanical properties: Part I: Powder preparation and compaction, Powder Technol. 126 (2002) 65–74, http://dx.doi.org/10.1016/S0032-5910(02)00034-7.

[24] A. Castellanos, The relationship between attractive interparticle forces and bulk behaviour in dry and uncharged fine powders, Adv. Phys. 54 (2005) 263–376, http://dx.doi.org/10.1080/17461390500402657.

[25] M.F. Ashby, L.J. Gibson, Cellular Solids: Structure and Properties, section ed., Cambridge University Press, 1999.

[26] J.W. Cahn, Phase separation by spinodal decomposition in isotropic systems, J. Chem. Phys. 42 (1965) 93–99, http://dx.doi.org/10.1063/1.1695731.

[27] K. Ding, X. Xu, L. Tsang, Electromagnetic scattering by bicontinuous random microstructures with discrete permittivities, IEEE Trans. Geosci. Remote Sens. 48 (2010) 3139–3151, http://dx.doi.org/10.1109/TGRS.2010.2043953.

[28] S. Tan, C. Xiong, X. Xu, L. Tsang, Uniaxial effective permittivity of anisotropic bicontinuous random media using NMM3D, IEEE Geosci. Remote Sens. Lett. 13 (2016) 1168–1172, http://dx.doi.org/10.1109/LGRS.2016.2574759.

[29] C. Soyarslan, S. Bargmann, M. Pradas, J. Weissmüller, 3D stochastic bicontinuous microstructures: Generation, topology and elasticity, Acta Mater. 149 (2018) 326–340, http://dx.doi.org/10.1016/j.actamat.2018.01.005.

[30] A.P. Roberts, E.J. Garboczi, Computation of the linear elastic properties of random porous materials with a wide variety of microstructure, Proc. R. Soc. Lond. Ser. A Math. Phys. Eng. Sci. 458 (2002) 1033–1054, http://dx.doi.org/10.1098/rspa.2001.0900.

[31] H. Xiao, L.S. Chen, Hencky's elasticity model and linear stress–strain relations in isotropic finite hyperelasticity, Acta Mech. 157 (2002) 51–60, http://dx.doi.org/10.1007/BF01182154.

[32] C.M. Mast, Modeling Landslide-Induced Flow Interactions with Structures Using the Material Point Method (Ph.D. thesis), University of Washington, Seattle, 2013.

[33] G. Klár, T. Gast, A. Pradhana, C. Fu, C. Schroeder, C. Jiang, J. Teran, Drucker–prager elastoplasticity for sand animation, ACM Trans. Graph. 35 (2016) 1–12, http://dx.doi.org/10.1145/2897824.2925906.

[34] J. Gaume, T. Gast, J. Teran, A. van Herwijnen, C. Jiang, Dynamic anticrack propagation in snow, Nature Commun. 9 (2018) 3047, http://dx.doi.org/10.1038/s41467-018-05181-w.

[35] D. Sulsky, Z. Chen, H.L. Schreyer, A particle method for history-dependent materials, Comput. Methods Appl. Mech. Engrg. 118 (1994) 179–196, http://dx.doi.org/10.1016/0045-7825(94)90112-0.

[36] J. Brackbill, D. Kothe, H. Ruppel, Flip: A low-dissipation, particle-in-cell method for fluid flow, Comput. Phys. Comm. 48 (1988) 25–38, http://dx.doi.org/10.1016/0010-4655(88)90020-3.

[37] A. Stomakhin, C. Schroeder, L. Chai, J. Teran, A. Selle, A material point method for snow simulation, ACM Trans. Graph. 32 (2013).

[38] M. Steffen, R.M. Kirby, M. Berzins, Analysis and reduction of quadrature errors in the material point method (MPM), Internat. J. Numer. Methods Engrg. 76 (2008) 922–948, http://dx.doi.org/10.1002/nme.2360.

[39] L. Blatny, P. Berclaz, F. Guillard, I. Einav, J. Gaume, Microstructural origin of propagating compaction patterns in porous media, Phys. Rev. Lett. 128 (2022) 228002, http://dx.doi.org/10.1103/PhysRevLett.128.228002.

[40] E.C. Aifantis, On the microstructural origin of certain inelastic models, J. Eng. Mater. Technol. 106 (1984) 326–330, http://dx.doi.org/10.1115/1.3225725.

[41] I. Vardoulakis, E.C. Aifantis, Gradient dependent dilatancy and its implications in shear banding and liquefaction, Ing.-Arch. 59 (1989) 197–208, http://dx.doi.org/10.1007/BF00532250.

[42] N. Guo, J. Zhao, 3D multiscale modeling of strain localization in granular media, Comput. Geotech. 80 (2016) 360–372, http://dx.doi.org/10.1016/j.compgeo.2016.01.020.

[43] H. Wu, J. Zhao, N. Guo, Multiscale modeling of compaction bands in saturated high-porosity sandstones, Eng. Geol. 261 (2019) 105282, http://dx.doi.org/10.1016/j.enggeo.2019.105282.

[44] H. Wu, J. Zhao, W. Liang, Pattern transitions of localized deformation in high-porosity sand stones: Insights from multiscale analysis, Comput. Geotech. 126 (2020) 103733, http://dx.doi.org/10.1016/j.compgeo.2020.103733.

[45] H. Wu, J. Zhao, W. Liang, The signature of deformation bands in porous sandtones, Rock Mech. Rock Eng. 53 (2020) 3133–3147, http://dx.doi.org/10.1007/s00603-020-02100-8.

[46] A. Cicoira, L. Blatny, X. Li, B. Trottet, J. Gaume, Towards a predictive multi-phase model for alpine mass movements and process cascades, Eng. Geol. 310 (2022) 106866, http://dx.doi.org/10.1016/j.enggeo.2022.106866.

[47] Z. Chen, X. Wang, F. Giuliani, A. Atkinson, Microstructural characteristics and elastic modulus of porous solids, Acta Mater. 89 (2015) 268–277, http://dx.doi.org/10.1016/j.actamat.2015.02.014.

[48] F.A. Gilabert, J.-N. Roux, A. Castellanos, Computer simulation of model cohesive powders: Plastic consolidation, structural changes, and elasticity under isotropic loads, Phys. Rev. E 78 (2008) 031305, http://dx.doi.org/10.1103/PhysRevE.78.031305.

[49] T.W. Barraclough, J.R. Blackford, S. Liebenstein, S. Sandfeld, T.J. Stratford, G. Weinländer, M. Zaiser, Propagating compaction bands in confined compression of snow, Nat. Phys. 13 (2017) 272–275, http://dx.doi.org/10.1038/nphys3966.

[50] H. Löwe, M. Zaiser, S. Mösinger, S. Schleef, Snow mechanics near the ductile–brittle transition: compressive stick–slip and snow microquakes, Geophys. Res. Lett. 47 (2020) 1–9, http://dx.doi.org/10.1029/2019GL085491.

[51] V. Vajdova, T.-f. Wong, Incremental propagation of discrete compaction bands: Acoustic emission and microstructural observations on circumferentially notched samples of bentheim, Geophys. Res. Lett. 30 (2003) 1775, http://dx.doi.org/10.1029/2003GL017750.

[52] J.R. Valdes, F.L. Fernandes, I. Einav, Periodic propagation of localized compaction in a brittle granular material, Granul. Matter 14 (2011) 71–76, http://dx.doi.org/10.1007/s10035-011-0302-3.

[53] F. Guillard, P. Golshan, L. Shen, J.R. Valdes, I. Einav, Dynamic patterns of compaction in brittle porous media, Nat. Phys. 11 (2015) http://dx.doi.org/10.1038/nphys3424.

[54] Z.H. Tu, V. Shim, C. Lim, Plastic deformation modes in rigid polyurethane foam under static loading, Int. J. Solids Struct. 38 (2001) 9267–9279, http://dx.doi.org/10.1016/S0020-7683(01)00213-X.

[55] R.O. Ramseier, C.M. Keeler, The sintering process in snow, J. Glaciol. 6 (1966) 421–424, http://dx.doi.org/10.3189/S0022143000019535.

[56] D. Szabo, M. Schneebeli, Subsecond sintering of ice, Appl. Phys. Lett. 90 (2007) 151916, http://dx.doi.org/10.1063/1.2721391.

[57] I. Peinke, P. Hagenmuller, G. Chambon, J. Roulle, Investigation of snow sintering at microstructural scale from micro-penetration tests, Cold Reg. Sci. & Technol. 162 (2019) 43–55, http://dx.doi.org/10.1016/j.coldregions.2019.03.018.

[58] S. Bardenhagen, J. Guilkey, K. Roessig, J. Brackbill, W. Witzel, J. Foster, An improved contact algorithm for the material point method and application to stress propagation in granular material, CMES Comput. Model. Eng. Sci. 2 (2001) 509–522, http://dx.doi.org/10.3970/cmes.2001.002.509.

[59] M.A. Homel, E.B. Herbold, Field-gradient partitioning for fracture and frictional contact in the material point method, Internat. J. Numer. Methods Engrg. 109 (2017) 1013–1044, http://dx.doi.org/10.1002/nme.5317.

[60] L. Shenhav, D. Sherman, Fracture of 3D printed brittle open-cell structures under compression, Mater. Des. 182 (2019) 108101, http://dx.doi.org/10.1016/j.matdes.2019.108101.

[61] J. Zhang, G. Lu, Z. You, Large deformation and energy absorption of additively manufactured auxetic materials and structures: A review, Composites B 201 (2020) 108340, http://dx.doi.org/10.1016/j.compositesb.2020.108340.

[62] J. Simo, Algorithms for static and dynamic multiplicative plasticity that preserve the classical return mapping schemes of the infinitesimal theory, Comput. Methods Appl. Mech. Engrg. 99 (1992) 61–112, http://dx.doi.org/10.1016/0045-7825(92)90123-2.

[63] A. Pradhana, Multiphase Simulation using Material Point Method (Ph.D. thesis), UCLA, 2017.

[64] C. Jiang, C. Schroeder, A. Selle, J. Teran, A. Stomakhin, The affine particle-in-cell method, ACM Trans. Graph. 34 (2015) 1–10, http://dx.doi.org/10.1145/2766996.

[65] C. Jiang, C. Schroeder, J. Teran, An angular momentum conserving affine-particle-in-cell method, J. Comput. Phys. 338 (2017) 137–164, http://dx.doi.org/10.1016/j.jcp.2017.02.050.

[66] C. Fu, Q. Guo, T. Gast, C. Jiang, J. Teran, A polynomial particle-in-cell method, ACM Trans. Graph. 36 (2017) 1–12, http://dx.doi.org/10.1145/3130800.3130878.

[67] Z. Qu, M. Li, F. De Goes, C. Jiang, The power particle-in-cell method, ACM Trans. Graph. 41 (2022) 1–13, http://dx.doi.org/10.1145/3528223.3530066.

[68] W.A. Olsson, Quasistatic propagation of compaction fronts in porous rock, Mech. Mater. 33 (2001) 659–668, http://dx.doi.org/10.1016/S0167-6636(01)00078-3.

[69] C. Park, S. Nutt, Anisotropy and strain localization in steel foam, Mater. Sci. Eng. A 299 (2001) 68–74, http://dx.doi.org/10.1016/S0921-5093(00)01418-0.

[70] R. Katsman, E. Aharonov, H. Scher, Numerical simulation of compaction bands in high-porosity sedimentary rock, Mech. Mater. 37 (2005) 143–162, http://dx.doi.org/10.1016/j.mechmat.2004.01.004.